

FIG. 2. Example of consensus system showing *AISync*. (a) Symmetric network of  $N = 3$  homogeneous nodes, each with  $L = 2$  subnodes coupled by a directed link (from subnode  $i''$  to  $i'$ ). (b) The same network but with heterogeneous nodes, in which the direction of the internal sublink in the (light) cyan node is the opposite of that in the (dark) green nodes. In both (a) and (b) we show the corresponding node-level visualization of the network at the top right. (c) Stability region (shaded gray) for the consensus dynamics. All the transverse modes for the homogeneous system in (a) are unstable (red squares), while those for the heterogeneous system in (b) are stable (blue dots).

### B. Coupled Lorenz oscillators

An example of nonlinear system exhibiting *AISync* is shown in Fig. 3. The network structure is symmetric and has  $N = 3$  nodes and  $K = 2$  types of links representing sublink patterns in the clockwise and counterclockwise directions in Fig. 3(a). Each node consists of  $L = 2$  subnodes, each of which is a chaotic Lorenz oscillator. The two subnodes are connected by a sublink, the direction of which determines the node type. This gives rise to two node types, and there are four possible distinct combinations of node types for the network—two homogeneous and two heterogeneous. The system has two parameters,  $a$  and  $b$ , representing the coupling strength of internal and external sublinks, respectively. We seek to determine for which values of  $a$  and  $b$  the system exhibits *AISync*.

In Fig. 3(b), we show  $\Psi_-$  (red) and  $\Psi_+$  (blue) as functions of  $a$  and  $b$ , where  $\Psi_-$  ( $\Psi_+$ ) are defined to be the smaller value of  $\Psi$  between the two possible homogeneous (heterogeneous) systems. In the region shaded purple (where  $\Psi_+ > 0$  and  $\Psi_- < 0$ ), the synchronous state  $\mathbf{x}_\ell^{(i)}(t) = \mathbf{s}(t)$ ,  $\forall i, \ell$  is stable for at least one of the heterogeneous systems, but unstable for both homogeneous systems. We further verify in this region that the other possible forms of synchronous states,  $\mathbf{x}_\ell^{(i)}(t) = \mathbf{s}_\ell(t)$ ,  $\forall i, \ell$ , are unstable for both homogeneous systems (through extensive numerical simulation—see Appendix E for details). This establishes conditions (C1) and (C2), thus

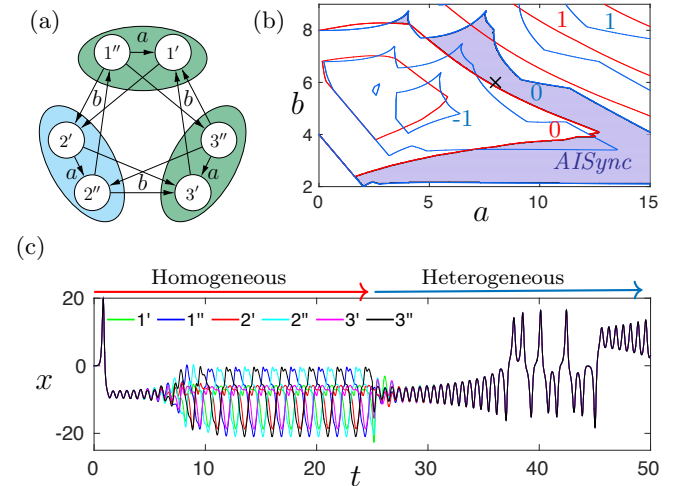


FIG. 3. Example of coupled Lorenz systems showing *AISync*. (a) Symmetric network of  $N = 3$  nodes, each with  $L = 2$  directionally coupled subnodes of Lorenz oscillators. Here we show an instance of a heterogeneous system in which the sublink direction in one node (cyan) is different from the other two (green). (b) Contour plots of  $\Psi_-$  (red) for the case of homogeneous nodes (all-green or all-cyan nodes) and  $\Psi_+$  (blue) for heterogeneous nodes (one or two green nodes). The shaded region corresponds to *AISync* systems, for which  $\Psi_- > 0$  and  $\Psi_+ < 0$ . (c) Sample trajectory of the system for  $a = 8$  and  $b = 6$  [cross symbol in (b)], exhibiting *AISync*. The first component  $x_1$  of the Lorenz oscillator state vector is shown for all  $n = 6$  subnodes.

confirming that the system exhibits *AISync* in the purple region. The *AISync* behavior of the system for a specific combination of  $a$  and  $b$  is illustrated by the sample trajectory in Fig. 3(c), which diverges from synchrony while the nodes are kept homogeneous, but re-synchronizes spontaneously after the nodes are made heterogeneous.

### C. Coupled electro-optic systems

We now present an experimentally testable *AISync* system based on the discrete-time model of the electro-optic system implemented in Refs. [16, 27] and given by

$$x_i^{t+1} = \left[ f(x_i^t) - \sum_j \tilde{L}_{ij} f(x_j^t) + \delta \right] \bmod 2\pi, \quad (6)$$

where  $f(x) = \beta I(x)$  determines the isolated subnode dynamics and also serves as the coupling function. Here,  $I(x) = (1 - \cos x)/2$  is the normalized optical intensity,  $\beta = 1.7\pi$  is the self-feedback strength,  $\delta = 0.2$  is the offset introduced to suppress the trivial solution  $x_i = 0$ , and  $\tilde{L}_{ij}$  is the weighted graph Laplacian [weights controlled by parameters  $a$  and  $b$ , as shown in Fig. 4(a–c)].

Figure 4 shows an example of *AISync* using these electro-optic maps as subnodes. The internal connections are chosen from the quaternary set (no sublink, one directed sublink in either direction, and directed sublinks

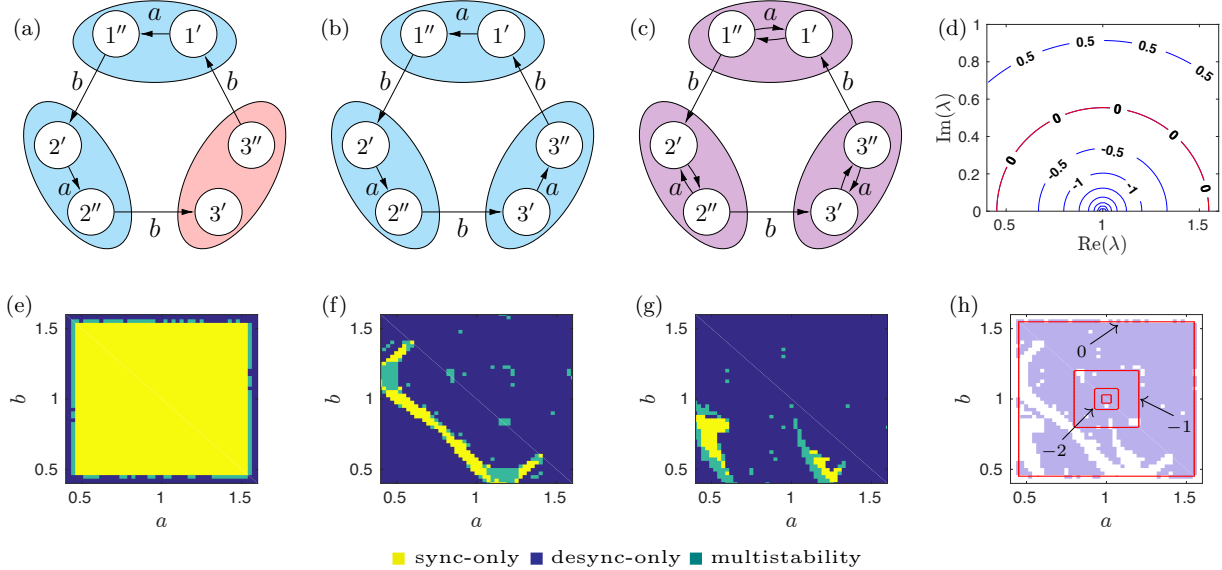


FIG. 4. Example of coupled electro-optic systems showing *AISync*. (a–c) Networks with heterogeneous (a) and homogeneous (b,c) nodes. (d) Stability function  $\psi(\lambda)$  for the electro-optic system. (e–g) Numerical results indicating where each system in (a–c) is synchronizable in the parameter space. Each pixel is categorized into three classes according to 24 independent simulations from random initial conditions (see text for details). (h) The *AISync* region (shaded purple), which is the union of yellow and green regions in (e) minus the analogous unions in (f) and (g). The red contours encode the MTLE for the heterogeneous system.

in both directions). When the same choice is made for all internal connections, this leads to four different homogeneous systems, but two of them have  $\lambda_2 = 0$  (not synchronizable), leaving only two homogeneous systems to consider [Figs. 4(b) and (c)]. For comparison, we take the heterogeneous system in Fig. 4(a), which forms a directed chain network in its monolayer representation. Each of the three systems [Figs. 4(a–c)] has a companion plot showing under what parameters the nodes are synchronizable [Figs. 4(e–g)]. In the latter panels, each pixel is generated from 24 independent simulations run from random initial conditions. The pixels are then color-coded according to how many times a fully synchronized state was reached after 2500 iterations (“sync-only”: 24 times; “desync-only”: 0 times; “multistability”: all other cases). Here we consider a trajectory to be fully synchronized if the synchronization error  $e$  defined in Eq. (D1) and averaged over the last 100 iterations falls below  $10^{-3}$ . It is worth noting that, in this example, when a homogeneous system is synchronizable the synchronous state is always in the form of cluster synchronization among subnodes (those indexed with prime and double prime form two separate synchronized clusters), since complete synchronization among subnodes is always unstable for both homogeneous systems.

Figure 4(d) shows the stability function  $\psi(\lambda)$  for the electro-optic subnode dynamics and coupling function, which has a bounded stable region. The lines are quite dense inside the stable region, meaning that the stability landscape is steep there and the function reaches very deep negative values. This is confirmed in Fig. 4(h),

where the *AISync* regions are shaded purple, with the MTLE of the synchronous state for the heterogeneous system shown as red contour lines.

#### D. Other examples

The three *AISync* systems considered in this section include both linear and nonlinear coupling functions, as well as discrete- and continuous-time dynamics. While they provide *AISync* examples with directed network structures and bounded stability regions, we also demonstrate *AISync* for systems with unbounded stability region (Supplemental Material Sec. S1), and for systems with undirected network structure (Supplemental Material Sec. S2).

#### VI. PROPENSITY FOR *AISync*

But how often does a network structure support *AISync*? To systematically address this question, we use the spread  $\sigma$  of the eigenvalues of the Laplacian matrix  $\tilde{L}$  for the monolayer network representation, which is a measure of synchronizability [8] defined by  $\sigma^2 := \sum_{j=2}^n |\lambda_j - \bar{\lambda}|^2 / [d^2(n-1)]$ , where  $d := \sum_{j=1}^n \tilde{L}_{jj} / n$  and  $\bar{\lambda} := \sum_{j=2}^n \lambda_j / (n-1)$ . A smaller  $\sigma$  indicates higher synchronizability. Given an external sublink structure corresponding to a symmetric network, we compare the minimum spread  $\sigma_-$  among all systems with homoge-

	$N = 3$	$N = 4$	$N = 5$
symmetric networks			
$Q$ (optimal)	9	14	21
$Q(r > 0.2)$	11	81	254
$Q(r > 0.05)$	29	318	2154
$B(r > 0.2)$	11	101	204
$B(r > 0.05)$	31	400	2406

TABLE I. Number of isomorphically distinct *AISync*-favoring networks, listed for  $N = 3, 4, 5$  nodes and  $L = 2$  layers (with  $a = b = 1$  to enable counting). The numbers are given for both binary (B) and quaternary (Q) choices of internal sublink configurations, as well as for different *AISync* strength (as measured by  $r$  defined in the text). The network diagrams encode all possible symmetric networks of a given size.

neous  $F^{(i)}$  to the corresponding minimum  $\sigma_{\neq}$  among all systems with strictly heterogeneous  $F^{(i)}$ . We call the structure *AISync-favoring* if  $\sigma_{\neq} < \sigma_+$ , which indicates that heterogeneous  $F^{(i)}$  can make the system easier to synchronize than any homogeneous  $F^{(i)}$ . As a measure of how strongly the structure supports *AISync*, we define  $r := 1 - \sigma_{\neq}/\sigma_+ \leq 1$ , where  $r > 0$  indicates an *AISync*-favoring structure, and  $r = 1$  implies  $\sigma_{\neq} = 0$  (i.e., there is a heterogeneous system with optimal synchronizability). For example, the structure in Fig. 3 has  $\sigma_+ \approx 0.56$  and  $\sigma_{\neq} \approx 0.33$ , and  $r \approx 0.41$ .

Using this *AISync* strength  $r$ , we first enumerate all networks of a given size supporting *AISync* (Table I). For each  $N$ , we generate one or more diagrams representing all  $N$ -node symmetric networks, which are shown in the first row of Table I for  $N = 3, 4, 5$ . In these diagrams, each color indicates a set of links that, in any given symmetric network, must all exist together and be of the same type or not exist at all (noting that links from different sets can be of the same type). For example, there are three distinct symmetric networks for  $N = 3$ : a directed ring (cyan or black links), an undirected ring (cyan and black links of the same type), and the superposition of two directed rings in opposite directions (cyan and black links of different types; as in Fig. 3). For a given symmetric network derived from these diagrams, we choose the external sublink pattern for each link type from all possible ways of connecting a subnode pair to another. For the internal sublink patterns, we use either the binary or quaternary choices, where each node has one directed sublink (in either direction) in the binary case, while all four possibilities are allowed in the quaternary case. The rest of Table I lists the total numbers of isomorphically distinct external sublink structures with  $r > 0.05$ ,  $r > 0.2$ , and (optimal)  $r = 1$ ; see Supplementary Tables S1 and S2 for all optimal networks with  $N = 3$  and 4, respectively.

Table II extends the first row in Table I, showing the

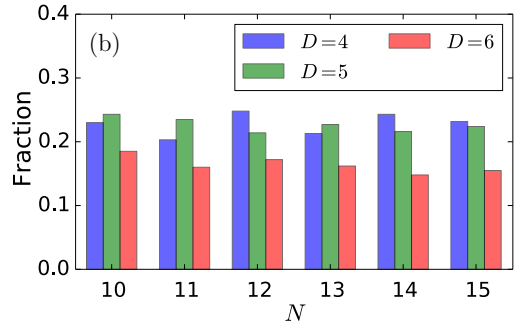
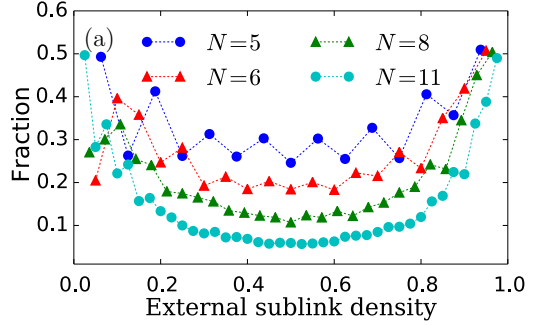


FIG. 5. Statistics on the prevalence of *AISync*-favoring networks. Shown as functions of (a) external sublink density and (b) network size  $N$ . Both panels show the fraction of systems with *AISync* strength  $r > 0.05$  among those with circulant network structures, where the external sublink density is given by  $D/[L^2(N - 1)]$ , and  $D$  is the number of external sublinks received by a node (which is the same for all nodes).

symmetric network diagrams for  $N = 6, 7$ , and  $8$ . In each row, the leftmost diagram is the full representation as in Table I, which is decomposed into multiple components (the partial diagrams in the same row) to make them more clearly visible. The partial diagrams with the same background color indicate identical components appearing in multiple rows. Thus, for  $N = 6$ , we have four different diagrams (rows), each with a different combination of components. There is only one diagram for  $N = 7$ , while we show one representative diagram out of twelve in the case of  $N = 8$ .

Figure 5 shows the statistics of *AISync*-favoring networks. For numerical feasibility, we focus on those systems whose network structure is a directed circulant graph with multiple link types (which covers all symmetric networks if  $N$  is a prime number). Sampling uniformly within this class (Appendix F), we observe that significant fraction of external sublink structures are *AISync*-favoring over a range of external sublink densities [Fig. 5(a)] and network sizes [Fig. 5(b)]. We also observe that sparse and dense structures favor *AISync* more often than medium-density ones, despite the expectation that the effect of internal sublink heterogeneity would be smaller with higher external sublink density. This phenomenon is further explored in Appendix G by establishing the approximate left-right symmetry in Fig. 5(a).